

Article

Immobilized TiO₂/ZnO Sensitized Copper (II) Phthalocyanine Heterostructure for the Degradation of Ibuprofen under UV Irradiation

Chukwuka BethelAnucha ^{1,*}, Ilknur Altin ^{1,*}, Emin Bacaksiz ², Ismail Degirmencioglu ¹,
Tayfur Kucukomeroglu ², Salih Yilmaz ³ and Vassilis N. Stathopoulos ⁴

¹ Department of Chemistry, Karadeniz Technical University, 61080 Trabzon, Turkey; ismail61@ktu.edu.tr

² Department of Physics, Karadeniz Technical University, 61080 Trabzon, Turkey; eminb@ktu.edu.tr (E.B.); tayfun@ktu.edu.tr (T.K.)

³ Department of Materials Engineering, Faculty of Engineering, Adana Alparslan Türkeş Science and Technology University, 01250 Adana, Turkey; slh_yilmaz@yahoo.com.tr

⁴ Laboratory of Chemistry and Materials Technology, General (Core) Department, National and Kapodistrian University of Athens, Psachna Campus, 34400 Evia, Greece; vasta@uoa.gr

* Correspondence: C.B.Anucha@ktu.edu.tr (C.B.A.); ilknurtatlidil@ktu.edu.tr (I.A.)

Abstract: Photocatalytic coatings of TiO₂/ZnO/CuPc were developed on stainless steel substrates by subsequent sol gel dip coating for TiO₂, spray pyrolysis for ZnO, and spin coating for copper (ii) phthalocyanine (CuPc) deposition. The latter compound was successfully prepared using a Schiff-based process. The materials and coatings developed were characterized by X-ray diffraction (XRD), Fourier transform infrared (FTIR) spectroscopy, scanning electron microscopy with attached energy dispersive spectroscopy (SEM-EDS), UV-Vis spectroscopy, room temperature photoluminescence (RTPL) spectroscopy, H1-nuclear magnetic resonance (¹H-NMR) spectroscopy, C13-nuclear magnetic resonance (¹³C-NMR) spectroscopy, and matrix-assisted laser desorption/ionization-time of flight (MALDI-TOF) mass spectrometry (MS). The as-deposited TiO₂/ZnO/CuPc on stainless steel retained in pristine state the structural and morphological/spectroscopic characteristics of its respective components. Estimated energy band gap values were 3.22 eV, 3.19 eV, 3.19 eV for TiO₂, ZnO, TiO₂/ZnO respectively and 1.60 eV, 2.44 eV, and 2.92 eV for CuPc. The photocatalytic efficiency of the fabricated TiO₂/ZnO/CuPc coatings was tested toward ibuprofen (IBF). After 4 h irradiation under 365 nm UV, an increased degradation of about 80% was achieved over an initial 5 mg/L ibuprofen (IBF). This was much higher compared to about 42% and 18% IBF degradation by TiO₂/ZnO and TiO₂ thin film, respectively. In all cases, the stability of the best-performing photocatalyst was investigated showing a small decline to 77% of IBF degradation after the 5th cycle run. The effect of pH, reactive oxygen species (ROS) probe, shed light on a possible catalytic mechanism that was suggested.

Keywords: heterogeneous photocatalyst; TiO₂; ZnO; copper (ii) phthalocyanine (CuPc), sensitization; thin film; contaminant of emerging concern (CEC), ibuprofen



Citation: BethelAnucha, C.; Altin, I.; Bacaksiz, E.; Degirmencioglu, I.; Kucukomeroglu, T.; Yilmaz, S.; Stathopoulos, V.N. Immobilized TiO₂/ZnO Sensitized Copper (II) Phthalocyanine Heterostructure for the Degradation of Ibuprofen under UV Irradiation. *Separations* **2021**, *8*, 24. <https://doi.org/10.3390/separations8030024>

Academic Editor: Victoria Samanidou

Received: 3 January 2021

Accepted: 1 February 2021

Published: 26 February 2021

Publisher's Note: MDPI stays neutral with regard to jurisdictional claims in published maps and institutional affiliations.



Copyright: © 2021 by the authors. Licensee MDPI, Basel, Switzerland. This article is an open access article distributed under the terms and conditions of the Creative Commons Attribution (CC BY) license (<https://creativecommons.org/licenses/by/4.0/>).

1. Introduction

Industrial revolution of the 19th century has tremendously improved the material progress of humankind and advanced the socio-economic livelihood [1]. Desire driven by more and better food and crop production, public health protection, and personal care practices facilitated commercial manufacturing of anthropogenic organic chemical compounds [1]. These compounds have been reported to breakdown slowly or to be persistent for a longer period and/or bioaccumulate [2,3]. A wide spectrum of these compounds is found with respect to their applications ranging from pesticides to pharmaceuticals and personal healthcare products (PPCPs), to organic solvents, to endocrine disrupting compounds (EDCs), to flame retardants, to artificial sweeteners, and other industrial chemical products [1–4]. Among these compounds, is a class of pollutants referred to

as contaminants of emerging concerns (CECs), anthropogenically synthesized organic chemical pollutants detected in natural water bodies at very low concentration levels [2–4]. Based on their perceived harmful effects on human and the environment, several treatment technologies for their abatement with an integrated approach as they elude conventional wastewater treatment plants (WWTPs) due to their recalcitrant nature have been studied [2,3]. The application of advanced oxidation processes (AOPs) for the removal of such organic compounds including the heterogeneous TiO₂-based photocatalysis approach for pollutant decontamination has gained huge interest and has been intensively studied [5].

Following pioneer works of Fujishima et al. in 1971–1972, intense research efforts has been focused on TiO₂ [5,6]. Culminating this research effort is extensive studies covering areas like photocatalytic splitting of water on TiO₂ electrodes, energy renewal and storage, and understanding of the fundamental processes involved in the photocatalytic efficiency of TiO₂ [5,7,8].

Environmental cleanup applications of TiO₂-based heterogeneous photocatalysis have been the most actively reported for the abatement of organic pollutants in air and wastewaters [7,8]. The many trade-offs of efficient photoactivity, high stability, low cost, and environmental friendliness of TiO₂ in comparison to many other semiconductor candidates for photocatalytic applications make it to stand out for industrial use [9].

In many cases of heterogeneous environmental catalysts, modifications are needed in order to improve their activity, stability, selectivity, working window, or the overall performance. This is achieved via compositional changes i.e., impregnation with an active or synergistic metal/oxide phase, doping or modifications in composition [10–12] or even structural changes via synthesis methods introducing a specific nanostructure [12–14]. In both strategies, the aim is to improve materials physicochemical properties crucial for a better catalytic performance. Such a concept is applied also for titania-based catalysts.

Despite the numerous advantages of TiO₂, its inability to achieve absorption in visible or even near visible wavelengths, rather large band gap, low quantum yield etc., have been some of its major practical drawbacks [9]. In order to address such drawbacks, strategies like doping, self-doping, 2D materials, quantum dots, metal co-catalyst deposition, composite realization with plasmonic materials, other semiconductors, graphene, surface dye sensitization etc., have been adopted [5,15]. Under this concept we recently reported the synthesis and characterization of B/NaF and silicon phthalocyanine-modified TiO₂. The as-prepared doped TiO₂-based materials were evaluated for the photocatalytic removal of a contaminant of emerging concern i.e., Carbamazepine as the model CEC [3].

One of the major issues in heterogeneous catalysts is the immobilization of the active phase over a suitable support. This is of high priority in liquid solid environmental catalytic systems. The latter is the major problem for TiO₂-based catalyst. A process using an immobilized catalyst is excluding the separation step in a liquid solid system. Thus, the catalyst is easily removed from the slurry in the end of the treatment [16]. Long working life and high efficiency of immobilized TiO₂-based heterogeneous photocatalyst is still a requirement. However, such forms of shaped catalysts have the potential of industrial scale-up in the degradation of organic pollutants in aqueous systems [17].

Various research groups have conducted studies of TiO₂-based photocatalysts on immobilization supports like glass, carbonaceous substances, zeolites, clay and ceramics, polymers, cellulose materials, and metallic agents as well immobilization techniques like spray pyrolysis, cold plasma discharge, dip coating, polymer assisted hydrothermal decomposition, radio frequency (RF) magnetron sputtering, photoetching, electrophoretic deposition, chemical vapor deposition (CVD), and solvent casting for the photodegradation of organic compound pollutants [18].

Among the extensively reported titania-based heterogeneous photocatalysis modification strategies, those aiming to advancements in enhancing the range of UV/visible-absorbing capabilities, reduced electron-hole charge recombination and eventually enhanced photocatalytic activity have been in the spotlight [19]. ZnO is another semiconducting material of attractive photocatalytic and optical properties. It has compatible

physicochemical properties with titania, and therefore has been studied in the form of TiO_2/ZnO or ZnO/TiO_2 coupled photocatalysts [19].

On the other hand, recent achievements in the development of TiO_2 -based, ZnO -based, Cu_2O -based etc., composite photocatalyst materials for solar driven water treatment applications have been reported [20,21]. TiO_2 coupling with some other metal oxides (e.g., WO_3 , Fe_2O_3 , Cu_2O , Bi_2O_3 , etc.), metal sulfides (e.g., CdS , CuS , MoS_2 , SnS_2 , etc.), silver-based semiconductors (e.g., Ag_3PO_4 , Ag_2O , etc.), graphene and graphene-like material composites, etc., have also been reported for the abatement of wide array of organic pollutants including contaminants of emerging concerns (CECs) [21]. For instance, Zhou et al. by the hydrothermal method prepared ZnO -reduced graphene oxide hybrid photocatalyst with a consistent high performance after 2-cycle deployment for the photocatalytic degradation of methylene blue (MB) under 365 nm irradiation [22]. $\text{Au}@\text{Cu}_2\text{O}$ core shell nanocrystals fabricated by Kuo et al. were tested as a dual-functional sustainable environmental applicable catalyst for methyl orange (MO) dye degradation and *Escherichia coli* (*E. coli*) inactivation under visible light and peroxidase conditions. It was fairly stable under both conditions after four cycles [23]. Hsu, et al. decorated TiO_2 nanowires with $\text{Au}@\text{Cu}_7\text{S}_4$ yolk @ shell nanocrystal as an all-day-active photocatalyst for environmental purification capable of degrading methyl orange (MO) under light illumination. It exhibited extended photocatalytic degradation activity even after the light switch off [24]. Apart from semiconductor oxides doping, dye sensitization approach has been an interesting concept for improved photoresponse in the degradation of organic pollutants by TiO_2 or other semiconductor-based photocatalyst materials [2,3,25]. Albay et al. synthesized copper (ii) phthalocyanine/ TiO_2 nanocomposite investigating both its photocatalytic activity and disinfection properties over Cr (VI) reduction and *Escherichia coli* (*E. coli*) inactivation near visible UV-A 365 nm irradiation source respectively [26]. Copper phthalocyanine sensitized TiO_2 tested under visible light irradiation for the degradation of methylene blue (MB) showed high activity of 100% MB removal and retained more than 80% of photocatalytic removal of the pollutant even after the 5th cycle of testing [27]. Vallejo et al. used TiO_2 films sensitized with Cu and Zn tetracarboxy phthalocyanine to degrade methylene blue (MB) under visible irradiation [28]. A copper phthalocyanine/reduced graphene oxide nanocomposite for efficient photocatalytic reduction of hexavalent chromium under simulated sun light has been reported [29]. In situ grown copper (ii) phthalocyanine-sensitized electrospun $\text{CeO}_2/\text{Bi}_2\text{MoO}_6$ nanofibers has been also reported to show remarkable photocatalytic activity under simulated sun light over tetracycline. The nanofibers maintained excellent recyclability and long-term stability [30].

Notwithstanding reasonable achievements over the past decades in TiO_2/ZnO -based heterogeneous photocatalysis for water purification applications, laudable progress has also been made generally in the area of the advancement of photocatalysis technology with current research efforts focused on heterostructure photocatalysts for improved sustainable applications. For instance, Seong Jun Mun and Soo-Jin Park in a short review examined graphitic carbon nitride ($\text{g-C}_3\text{N}_4$)—an attractive material for photocatalytic hydrogen production, communicating various rational design of their base materials aimed at addressing among other issues charge recombination during their application while also highlighting their recent achievements as applied hydrogen production photocatalysts [31]. Metal sulfide composite nanomaterials for photocatalytic hydrogen production has equally been examined with focused attention ranging from their key experimental parameters, in situ characterization methods, performances etc., on ways of how their heterogeneous, immobilized, and magnetically separable forms can deal with the problem of their rapid charge recombination [32]. Semiconductor heterostructure materials with attention on design principle, interfacial charge dynamics, and other factors of influence over their overall performance toward photoconversion applications in water splitting, CO_2 reduction, environmental purification, and photosynthesis have also been documented [33]. In order to understand more of the enhanced photocatalytic performance of composite materials with attributes not limited to synergistic effects only, Ge et al. took appraisal of current

developments in the design and fabrication of various composite photocatalyst materials for wastewater treatment applications [34].

In the present work the modification strategy of semiconductor doping together with phthalocyanine sensitization, is occupied. The preparation of TiO₂/ZnO/CuPc heterostructure immobilized on stainless steel is reported for the first time. Its photocatalytic ability for the degradation of ibuprofen (IBF), a contaminant of emerging concern (CEC), under UV light irradiation is also studied.

2. Materials and Methods

2.1. Chemicals and Reagents

Chemical reagents were of analytical grade, used as purchased from Sigma Aldrich (Darmstadt, Germany) without any further treatment. Chemicals used were titanium triethanolamine isopropoxide (TTIP), hydrochloric acid (HCl), ethanol, ZnCl₂, dimethyl formamide (DMF), ethanol, ethyl acetate, acetone, 4-nitrophthalonitrile, potassium carbonate, urea, copper (ii) acetate monohydrate. Milli-Q water has been used for the entire photocatalytic experimental studies.

2.2. Instrumentation and Methods

¹H/¹³C-NMR spectra were recorded on a Varian XL-400 NMR spectrometer (Brucker BioSpin MRI GmbH, Rheinstetten, Baden-Wurttemberg, Germany) in DMSO-d₆ and chemical shifts (δ) were reported relative to Me₄Si (tetramethyl silane) as internal standard. IR spectra were recorded on a Perkin-Elmer Spectrum One FT-IR spectrometer (Thermo Fisher Scientific, Leicestershire, UK). The mass spectra were measured with a Micromass Quattro LC/ULTIMA LC- MS/MS (Brucker Daltonik GmbH, Hamburg, Germany) spectrometer using chloroform–methanol as the solvent system for phthalonitrile (3) and with a MALDI-TOF MS (Brucker Microflex LT, Bremen, Germany) spectrometer in dihydroxybenzoic acid as MALDI matrix using nitrogen laser accumulating 50 laser shots for copper phthalocyanine (4). Melting points were measured by a Thermo Scientific 00590Q Fisher-Johns melting point apparatus, 220 VAC (Cole-Palmer, Brescia Cernusco Sul Naviglio, Milano, Italy). The ultraviolet-visible (UV–vis) absorption spectra were recorded on Perkin Elmer Lambda 25 UV–vis spectrophotometer at room temperature for the synthesized copper phthalocyanine (CuPc) and in transmittance mode for optical band gap measurement of the produced film structures. Room temperature photoluminescence (RTPL) measurements were performed through Dongwoo Optron PL device (Dongwoo Optron Inc., Gyeonggi-do, South Korea) with Xenon lamp as light source at an excitation wavelength of 280 nm in the wavelength interval of 330–850 nm. X-ray diffraction (XRD) was carried out using a Rigaku D/Max-III C diffractometer (RIGAKU, Corp; Tokyo, Japan) with CuK α radiation ($\lambda = 0.1541$ nm) over the range $2\theta = 10^\circ - 70^\circ$ at room temperature, operated at 35 kV and 25 mA at the rate of $3^\circ/\text{min}$ scan speed. Scanning electron microscopy (SEM-JEOL JSM-6610) (Carl Zeiss Microscopy, Hamburg, Germany) with attached energy dispersive x-ray spectroscopy (EDS) (Carl Zeiss SmartEDX, Hamburg, Germany) was employed for the determination of the morphology, microstructure, and composition of the produced film and layered heterostructures. For the copper (II) phthalocyanine (CuPc) synthesis, reactions have taken place under inert and oxygen-free nitrogen atmosphere.

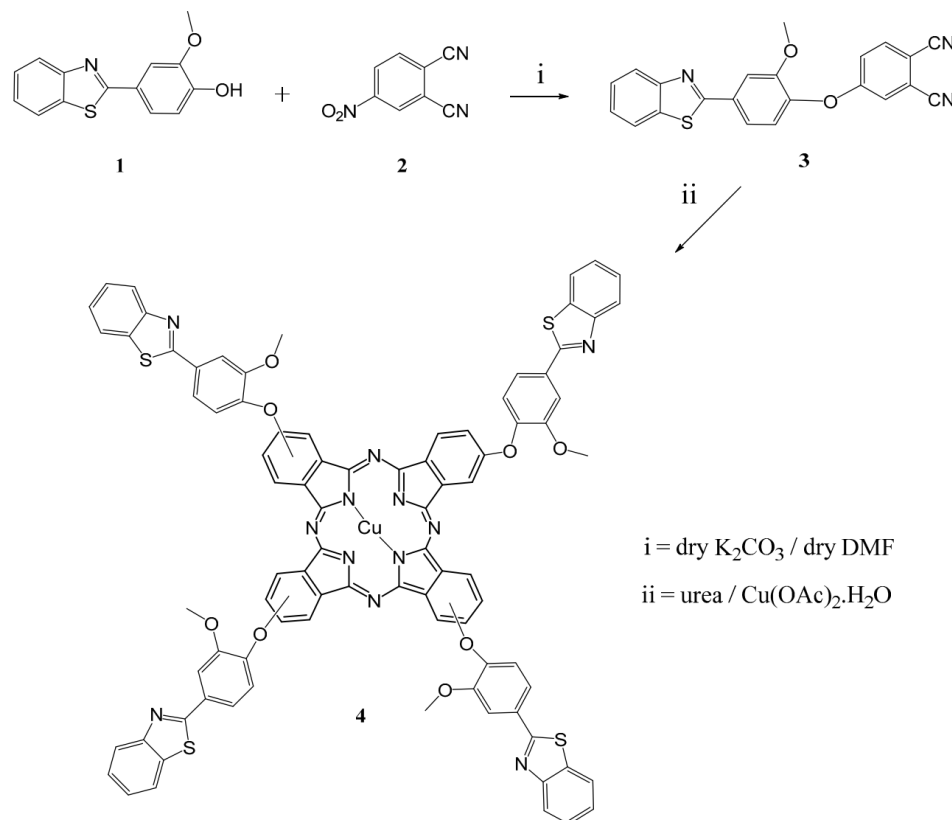
2.3. Synthesis and Characterization of Copper (II) Phthalocyanine (CuPc)

The synthesis procedure is described below in steps after preparing 4-(4-benzo[d]thiazol-2-yl)-2-methoxyphenoxy phthalonitrile and then the phthalocyanine compound.

- 4-(4-benzo[d]thiazol-2-yl)-2-methoxyphenoxy phthalonitrile (3)

As presented in Scheme 1, the starting materials: 4-(benzo[d]thiazol-2-yl)-2-methoxyphenol (1) (0.41 g, 1.58 mmol) synthesized according to literature [35] and commercially purchased 4-nitrophthalonitrile (2) (0.27 g, 1.58 mmol) were mixed in dry DMF (20 mL) to derive 4-(4-benzo[d]thiazole-2-yl)-2-methoxyphenoxy phthalonitrile (3). After half an hour, dry K₂CO₃ (0.54 g, 3.94 mmol) was added to this mixture in eight portions. The

reaction was continued at 50 °C for 4 days, then the mixture was poured into 200 mL ice-water. Crystallization of the compound was performed using ethanol. Yield: 0.60 g (98.4%). M.p.: 143–145 °C.



Scheme 1. The reaction pathway of CuPc (4).

FT-IR (ATR) $\nu_{\text{max}}/\text{cm}^{-1}$: 3125–3078 (Ar-CH), 2922–2851 (Alip.-CH), 2229 ($\text{C}\equiv\text{N}$), 1589–1517 ($\text{C}=\text{N}/\text{C}=\text{C}$), 1315, 1007, 841 (Ph-O-C).

$^1\text{H-NMR}$ (DMSO-d_6), (δ , ppm): 8.19–8.14 (d, 1H/Ar-H), 8.12–8.05 (t, 2H/Ar-H), 7.9–7.88 (bs, 1H/Ar-H), 7.8–7.77 (m, 1H/Ar-H), 7.76–7.71 (dd, 1H/Ar-H), 7.6–7.54 (t, 1H/Ar-H), 7.52–7.46 (t, 1H/Ar-H), 7.44–7.35 (m, 2H/Ar-H), 3.9–3.87 (s, 3H/- OCH_3).

$^{13}\text{C-NMR}$ (DMSO-d_6), (δ , ppm): 166.83 ($\text{C}=\text{N}$), 161.24, 153.93, 151.98, 144.04, 136.63, 135.13, 132.32, 127.27, 126.18, 123.66, 123.42, 122.88, 121.88, 121.43, 121.32, 117.05, 116.39 ($\text{C}\equiv\text{N}$), 115.86 ($\text{C}\equiv\text{N}$), 111.99, 108.52, 56.55 (- CH_3). MS (ESI), (m/z): Calculated; 383.43, Found; 383.07 [M] $^+$.

- 2,9,16,24-tetrakis [4-(1,3-benzothiazol-2-yl)-2-methoxyphenoxy]-29H,31H-(2-)- $\kappa^2\text{N}^{29}$, N^{31}CuPc (4)

To synthesize the phthalocyanine compound (4) (Scheme 1), the phthalonitrile compound 3 (0.1 g, 0.26 mmol), urea (0.031 g, 0.52 mmol), and $\text{Cu}(\text{OAc})_2 \cdot \text{H}_2\text{O}$ (0.026 g, 0.13 mmol) were mixed in a flask and the reaction was continued at 220 °C for half an hour. The crude solid product was washed with ethanol, ethyl acetate, and acetone, then refined by column chromatography (chloroform-methanol/100–10). Yield: 0.1 g (24.4%). M.p. > 300 °C.

FT-IR (ATR) $\nu_{\text{max}}/\text{cm}^{-1}$: 3059–3002 (Ar-CH), 2966–2937 (Alip. -CH), 1598–1513 ($\text{C}=\text{N}/\text{C}=\text{C}$), 1267, 1092, 868 (Ph-O-C).

UV-vis (THF) $\lambda_{\text{max}}/\text{nm}$ [$10^{-5}\epsilon$, $\text{dm}^3\text{mol}^{-1}\text{cm}^{-1}$]: 350 (3.81), 611 (4.37), 678 (4.96).

MALDI-TOF-MS (m/z) Calculated for $\text{C}_{88}\text{H}_{52}\text{CuN}_{12}\text{O}_8\text{S}_4$: 1597.24; Found: 1597.34 [M] $^+$.

2.4. Preparation of Film Coatings

Stainless steel rectangular coupons of 20 mm *times* 50 mm dimensions were used as substrates for the thin films deposition. TiO₂ thin films were deposited on the substrates by a sol-gel dip coating route. Prior to deposition, the substrate was cleaned with acetone, ethanol, and distilled water in an ultrasonic bath for 10 min. Then, the substrate was dried under airflow. To prepare TiO₂ thin film, titanium (IV) (triethanolamine) isopropoxide solution was used as a titanium source. Total of 8.4 mL of titanium (IV) (triethanolamine) isopropoxide solution was dissolved in 150 mL of pure ethanol. Then 500 µL of distilled water and 220 µL of HCl acid were added to the ethanolic solution. The resulting solution was kept under stirring for 6 h. Afterwards, the substrate was dip-coated using the prepared solution. The dip coating was followed by a subsequent annealing at 350 °C for 10 min. The procedure was repeated three times. The coated substrate was finally annealed at 450 °C for 10 h in ambient air to form a TiO₂ thin film on the stainless steel substrate.

ZnO was deposited on the TiO₂-coated stainless steel substrate for a bilayer formed by a vertically mounted home-made spray pyrolysis equipment [36]. The experimental details of this method can be found in our earlier work [36]. According to this method ZnO of columnar structure are expected to form. Namely, zinc chloride (ZnCl₂) (0.1 M) was dissolved in 100 mL of distilled water to prepare the stock solution. The prepared solution was then sprayed onto the TiO₂-coated stainless steel substrate kept at a temperature of 475 °C. Spray pyrolysis deposition was carried out for 1 h. During the topcoat growth process, the distance between nozzle and the substrate was 10 cm. The substrate was vortexed at 10 rpm. The spray rate was adjusted as 5 mL/min by means of compressed air pump. A visual inspection confirmed that the surface of the TiO₂/ZnO coated stainless steel substrate was covered homogenously. The obtained topcoat layer on the substrate was finally annealed at 450 °C for 10 h in ambient air.

The CuPc was added on the TiO₂/ZnO coating by spin coating technique at 4000 rpm of a CuPc solution in DMF (30 mg CuPc in 6 mL of DMF). Four depositions were applied. After each deposition, annealing at 250 °C for 10 min was made. Each of the as-deposited structures of TiO₂ thin film, TiO₂/ZnO topcoat, and TiO₂/ZnO/CuPc heterostructure were finally annealed at 300 °C for 30 min in air ambient and confirmed by XRD. The as-produced TiO₂ thin film, TiO₂/ZnO topcoat, and TiO₂/ZnO/CuPc layered structure on stainless steel substrates were characterized and evaluated for their photocatalytic activity over ibuprofen degradation.

2.5. Photocatalytic Measurements

The photocatalytic performance of the synthesized photocatalyst materials was evaluated toward the degradation of ibuprofen (IBF) under 365 nm irradiation. An internal 200 degree reflector for optimal efficiency (99.9%), UV-A, and visible blue wavelength in the range of 300 nm to 475 nm spectral power distribution was fabricated inhouse with a 5 Philips Mercury (Hg) lamps: TL-K 40W/10R ACTINIC BL REFLECTOR, (Germany) and employed for the photocatalytic tests of the synthesized materials. The irradiation experiments were executed at 365 nm cut-off filter. The intensity of the light source measured with solar power meter Lafayette SPM-7, (Italy) was 1.2 W/cm².

Stainless steel supports (20 mm × 50 mm) coated with films of TiO₂, TiO₂/ZnO, and TiO₂/ZnO/CuPc were immersed in quartz cells containing 40 mL of a 5 mg/L IBF working suspension, and kept under mechanical agitation during the irradiation. For simplicity, thin film samples over stainless steel coupons were named: TiO₂, TiO₂/ZnO, and TiO₂/ZnO/CuPc. Prior to irradiation, suspension was stirred in the dark for 30 min to establish adsorption–desorption equilibrium while irradiation stability was achieved. Unmodified natural pH values of the materials working suspensions of TiO₂, TiO₂/ZnO, TiO₂/ZnO/CuPc were 6.65, 6.64, and 6.50 respectively. Finally, all other experimental tests were carried out at pH 6.50 of TiO₂/ZnO/CuPc as the best performing photocatalyst composite according to the preliminary test. A distance of 30 cm between sample and light source was maintained throughout the experiments. At chosen time intervals, about 1 mL

sample aliquots were drawn from reactor cells, cooled and filtered through 0.45 μm CA filter for HPLC analysis. Monitoring of IBF degradation was executed on Kinetex 5 μm EVO C18, column 150 mm \times 4.6 mm Phenomenex (USA). Runtime was 15 min and eluents were 70% acetonitrile (ACN) and 30% acetic acid (hAc) with a flow rate of 0.2 mL.min⁻¹. IBF quantification was performed at 223 nm wavelength with a retention time of \sim 12 min.

The photocatalytic degradation process of IBF follows a pseudo first-order reaction kinetics with reaction rate of IBF estimated as a linear regression slope according to expressed Equation (1):

$$-\ln \frac{C}{C_0} = K_{\text{app}} t \quad (1)$$

where, k_{app} , C_0 , and C are apparent degradation rate constant, initial concentration, and concentration after time t , respectively.

3. Results and Discussion

3.1. Synthesis and Characterization of Copper (ii) Phthalocyanine (CuPc)

Scheme 1 represents the synthetic steps for the novel compounds (3–4). 4-(4-benzo[d]thiazol-2-yl)-2-methoxyphenoxy phthalonitrile (3) was prepared by the reaction between 4-(benzo[d]thiazol-2-yl)-2-methoxyphenol (1) and 4-nitrophthalonitrile (2).

In the ¹H-NMR spectrum of the thiazole-methoxyphenoxy substituted phthalonitrile (3) (supplementary information Figure S1), all aromatic protons of the molecule (3) occurred in the range 8.19–7.35 ppm. The ¹H-NMR results showed that the substitution reaction was performed successfully. The newly observed vibrations at 2229 cm⁻¹ in the IR spectrum and the signals at δ 116.39 and 115.86 ppm in the ¹³C-NMR spectrum (supplementary information Figure S2) confirmed that compound (3) has nitrile (C \equiv N) groups. In the mass spectrum, the 383.07 [M]⁺ peak confirmed the structure of phthalonitrile (3) (supplementary information Figure S3). The obtained spectral data are consistent with the literature on substituted phthalonitriles [2,37–39].

The compound (4) was obtained with a mixture of phthalonitrile (3), urea, and Cu(OAc)₂ · H₂O salt at 220 °C for half an hour. The disappearance of the (C \equiv N) vibration of compound (3) in the IR spectrum was the most important marker confirming the formation of the CuPc (4) molecule. The ¹H-NMR spectrum of CuPc could not be recorded because of the paramagnetic properties of the Cu²⁺ in the core of the phthalocyanine complex. In addition, the mass spectrum of compound (4) confirmed the structures with the 1597.34 [M]⁺ peak (supplementary information Figure S4). All spectral data are consistent with the literature on tetra substituted metallo-phthalocyanines [37–39].

UV-Visible Absorption of CuPc

From the UV–vis spectrum of the CuPc (Figure 1), Q-band was observed at around 678 nm with the shoulder at around 611 nm and the B band observed at around 350 nm. CuPc's Q and B bands were red-shifted compared to their metallophthalocyanine counterparts because of the electron-donating methoxy moiety in its structure [37–39]. These characteristic absorption bands were similar to the ones identified of silicon phthalocyanine in our recent study [3].

3.2. Characterization of Photocatalyst Structures

3.2.1. X-Ray Diffraction (XRD) Measurements

XRD patterns of TiO₂ thin film, TiO₂/ZnO topcoat, and TiO₂/ZnO/CuPc heterostructure grown on stainless steel substrates are shown in Figure 2. It is clearly seen that TiO₂ thin film produced on the substrate displays a low intensity peak of (101) corresponding to anatase TiO₂ structure according to the JCPDS card # 21-1272.

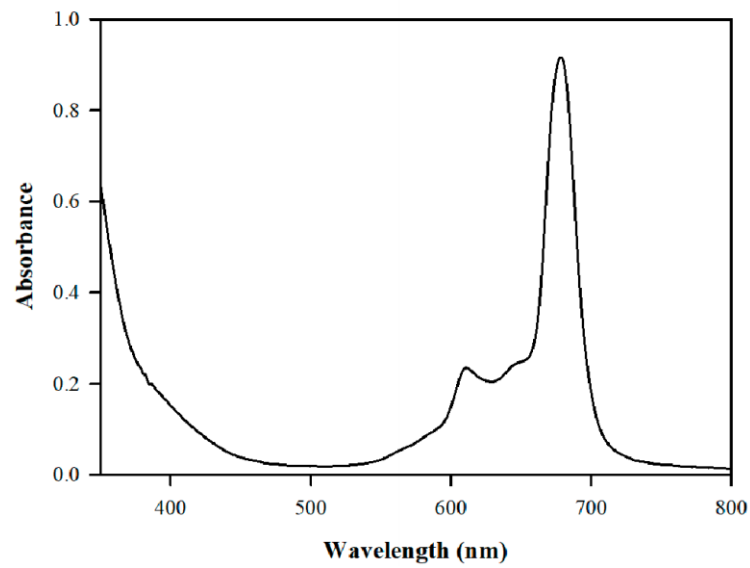


Figure 1. UV-vis spectrum of 1×10^{-5} M CuPc (4) in THF.

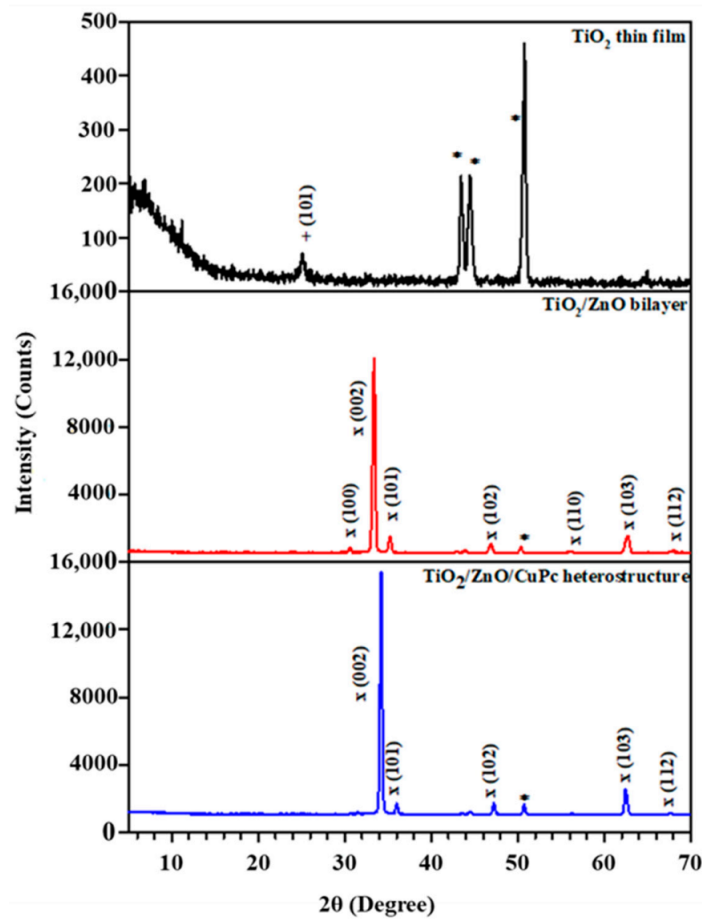


Figure 2. XRD patterns of TiO₂ thin film (black line), TiO₂/ZnO bilayer (red line), and TiO₂/ZnO/CuPc layered structure (blue line) on stainless steel substrates (Peaks *: substrate; +: TiO₂ anatase; x: ZnO).

Besides this peak, there seem some other peaks located in the pattern, originating from the metallic substrate (JCPDS card #00-031-0619). TiO₂/ZnO topcoat shows peaks at 2θ angles of 31.8°, 34.5°, 36.3°, 47.6°, 56.6°, 62.9°, and 68.0° with their respective reflection planes of (100), (002), (101), (102), (110), (103), and (112) indexed to hexagonal ZnO structure

with a JCPDS card #36-1451; and in agreement with the reported data [40]. Additionally, peaks coming from underlying layers of the anatase titania (101) are recorded in the TiO_2/ZnO sample (Figure 2). The existence of intense and narrow ZnO peaks in the pattern was also observed, meaning that the crystallinity of ZnO is good. The intensity of (002) peak is higher than that of the others, indicating a strong c-axis orientation. The lattice constants a and c of hexagonal ZnO layer, calculated through (100) and (002) diffraction peaks were determined to be 0.325 nm and 0.521 nm, respectively and agreed with reported literature values [41]. The $\text{TiO}_2/\text{ZnO}/\text{CuPc}$ heterostructure illustrates an XRD pattern that is similar to that of TiO_2/ZnO topcoat, except for the appearance of a not-so-prominent (101) peak of TiO_2 thin film in the diffractogram of the later. There seems no peak belonging to the CuPc layer which is due to very thin growth of it on the TiO_2/ZnO topcoat. Additionally, the coating of CuPc layer did not remarkably change XRD peak position of ZnO as can be observed (Figure 2).

3.2.2. Fourier Transform Infrared (FTIR) Analysis

The presented FTIR spectra in Figure 3, show absorption band at around 744 cm^{-1} attributed to stretching mode of Ti-O in the material film structures [42]. The peak band at around 870 cm^{-1} is attributed to Zn-O-Ti stretching mode while that identified at around 1080 cm^{-1} belongs to Ti-OH vibrations and possibly due to carbonates or carboxylic acid (C=O) stretching mode and or C=C stretching arising from the unsaturated precursors used for film production [3,19,42,43]. The presence of copper phthalocyanine (CuPc) led to stretching peak prominence at the identified absorption bands in comparison to TiO_2 and TiO_2/ZnO samples (Figure 3). The more noticeable a bit wider stretching absorption peak at around 1600 cm^{-1} in the $\text{TiO}_2/\text{ZnO}/\text{CuPc}$ sample compared to that of TiO_2 and TiO_2/ZnO is due to surface absorbed water molecules as the incorporated CuPc increased the surface area and hydrophilicity of the multilayer heterostructure [2,44].

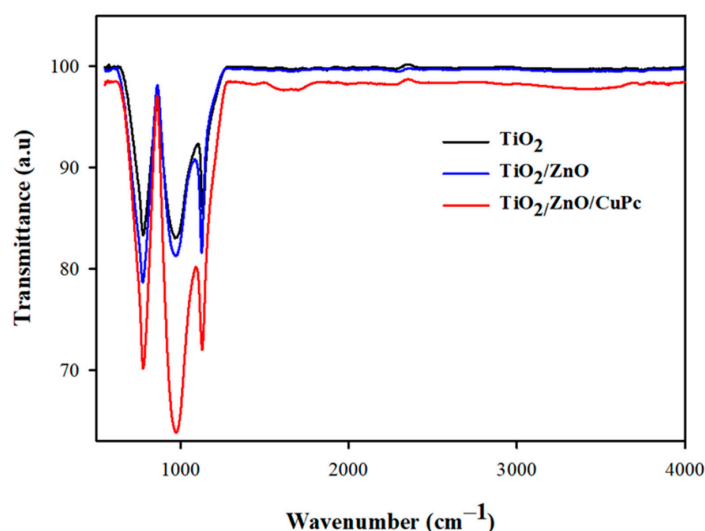


Figure 3. FT-IR spectra of TiO_2 thin film (black curve), TiO_2/ZnO bilayer (blue curve), and $\text{TiO}_2/\text{ZnO}/\text{CuPc}$ heterostructure (red curve) grown on quartz substrate.

3.2.3. Scanning Electron Microscopy (SEM)

Figure 4 shows the SEM images of TiO_2 thin film, TiO_2/ZnO topcoat, and $\text{TiO}_2/\text{ZnO}/\text{CuPc}$ heterostructure grown on stainless steel substrates. Top view and 60° tilted SEM images of TiO_2 thin films grown on stainless steel substrates are presented in Figure 4a,b, respectively. It is apparent from Figure 4a that the surface of stainless steel substrate is uniformly covered by TiO_2 thin films that grow in a smooth and compact surface without any pinholes. The distribution of grain sizes is not homogeneous throughout the surface. That is, their sizes range from nearly $5\text{ }\mu\text{m}$ to $40\text{ }\mu\text{m}$. The grains are distinctly separated from each other via some cracks. It can be pronounced that the cracks almost overlap with

the grain boundaries. As can be seen in Figure 4b, the average depth of these cracks is almost 0.19 nm. Such cracks were also observed by Khan and co-workers for ZnO/TiO₂ thin films synthesized by the sol-gel route [45]. The occurrence of cracks on the surface of TiO₂ thin films could be associated with the mismatch of the thermal expansion coefficient between the stainless steel substrate and the coatings, the thickness of TiO₂ thin films and the number of TiO₂ coatings applied and their respective degree of shrinkage upon drying and thermal treatment [46]. Figure 4c demonstrates the top view image of ZnO layer grown mostly as hexagonal rods on the TiO₂-coated stainless steel substrate. Their size distribution is not uniform throughout the surface. Although the surface has a compact structure, it does not seem smooth because there are some differences in the size of ZnO rods. This may result from the cracks observed among the grains that are filled by the ZnO rods. It is observed from the 60° tilted SEM image of TiO₂/ZnO bilayer (Figure 4d) that the mean thickness of ZnO rods is about 1.82 μm. The top view SEM image of TiO₂/ZnO/CuPc heterostructure in Figure 4e, implies that CuPc layer is uniformly covered on TiO₂/ZnO topcoat surface, which is not so thick.

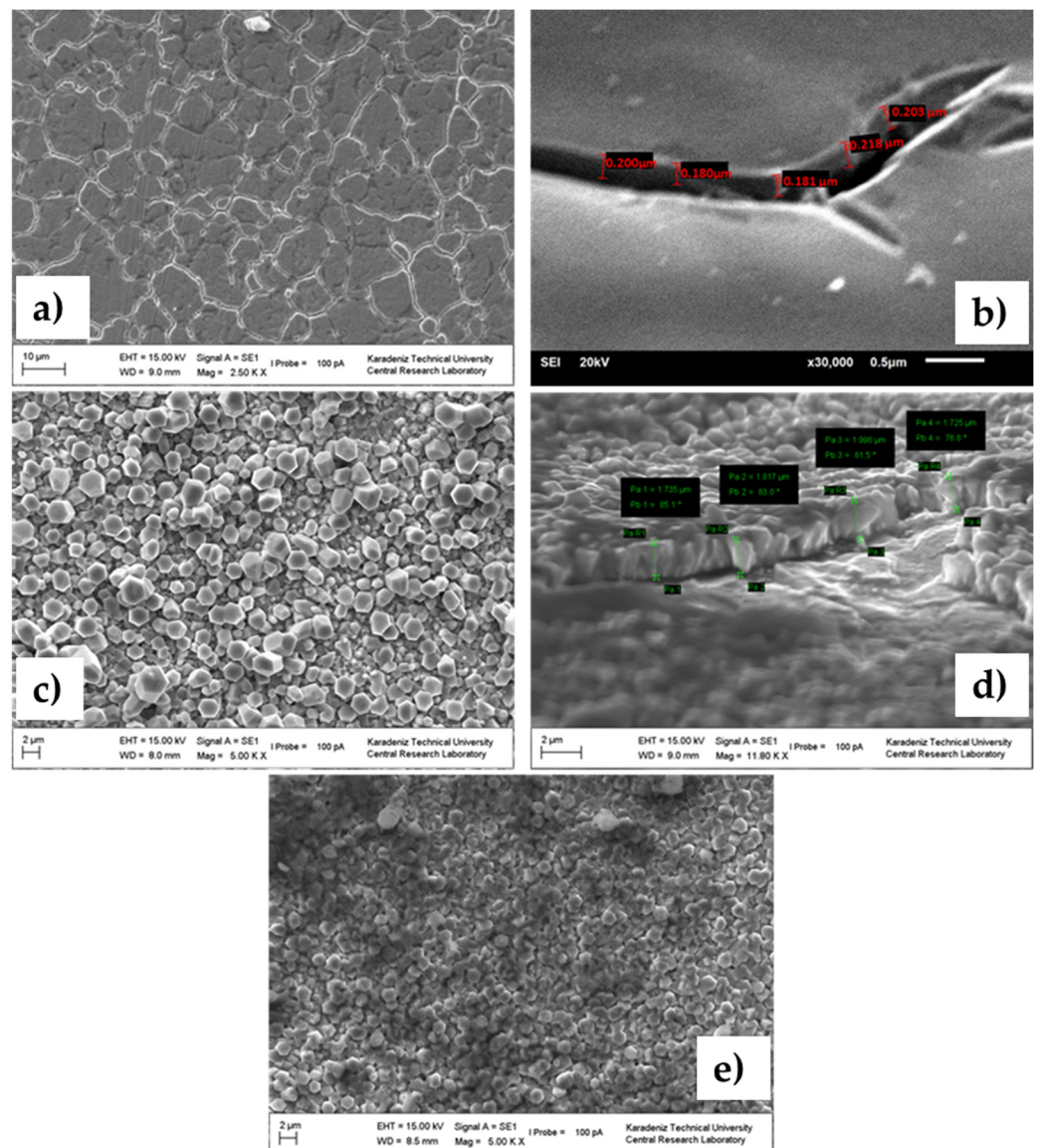


Figure 4. (a) Top view and (b) 60° tilted SEM images of TiO₂ thin film, (c) top view and (d) 60° tilted SEM pictures of TiO₂/ZnO bilayer structure, (e) top view SEM image of TiO₂/ZnO/CuPc heterostructure grown on stainless steel substrates.

As presented in Table 1, elemental ingredients of TiO₂/ZnO/CuPc heterostructure confirms the presence of O, Ti, Cu, and Zn elements in the heterostructure with no other impurities. It can also be seen that atomic concentration of Cu atoms is so low because of the formation of very thin CuPc layer. On the other hand, the top layer of ZnO rods is found Zn-rich and consequently O-deficient, indicating the existence of some intrinsic defects such as oxygen vacancy (V_o), zinc interstitials (Zn_i). Atomic density of Ti elements in the TiO₂/ZnO/CuPc heterostructure is the least, which may propose the thin growth of TiO₂ layer.

Table 1. Atomic concentration of O, Ti, Cu, and Zn in TiO₂/ZnO/CuPc heterostructure.

Element	Weight %	Atomic %
OK	15.40	42.62
TiK	0.32	0.30
CuK	0.60	0.42
ZnK	83.67	56.66

3.2.4. UV-Visible Spectroscopy (UV-Vis) Measurement

The energy band gap values of the grown structures on quartz substrates were estimated through Tauc's plot of $(\alpha h\nu)^2$ vs. $h\nu$ for ZnO, and TiO₂/ZnO (Figure 4a), and $(\alpha h\nu)^{1/2}$ vs. $h\nu$ for TiO₂ (Figure 5a), and CuPc (Figure 4b) by extrapolating the linear part of $(\alpha h\nu)^2$ and $(\alpha h\nu)^{1/2}$ equal to zero (Figure 5a,b). The obtained energy band gap values of TiO₂, ZnO, TiO₂/ZnO were 3.22 eV, 3.19 eV, 3.19 eV respectively and for the CuPc at 1.60 eV, 2.44 eV, and 2.92 eV for its respective measured absorption bands (Figure 5a,b). The obtained energy band gap of pure TiO₂ thin film at 3.22 eV, is in good agreement with data already reported in literature [47]. The energy band (E_g) gap value of 3.19 eV estimated for ZnO rods is well within the range reported of ZnO rods prepared by spray pyrolysis, which is lower than that of bulk ZnO (3.37 eV at room temperature). This red-shift could be probably due to important differences in the surface states [48]. On the other hand, estimated TiO₂/ZnO topcoat energy band gap of 3.19 eV was the same as that of ZnO rods. Upadhyay et al. produced ZnO:TiO₂ nanocomposite powders by the sol-gel method and found the band gaps of the nanocomposite materials in the range of 3.10–3.30 eV [49].

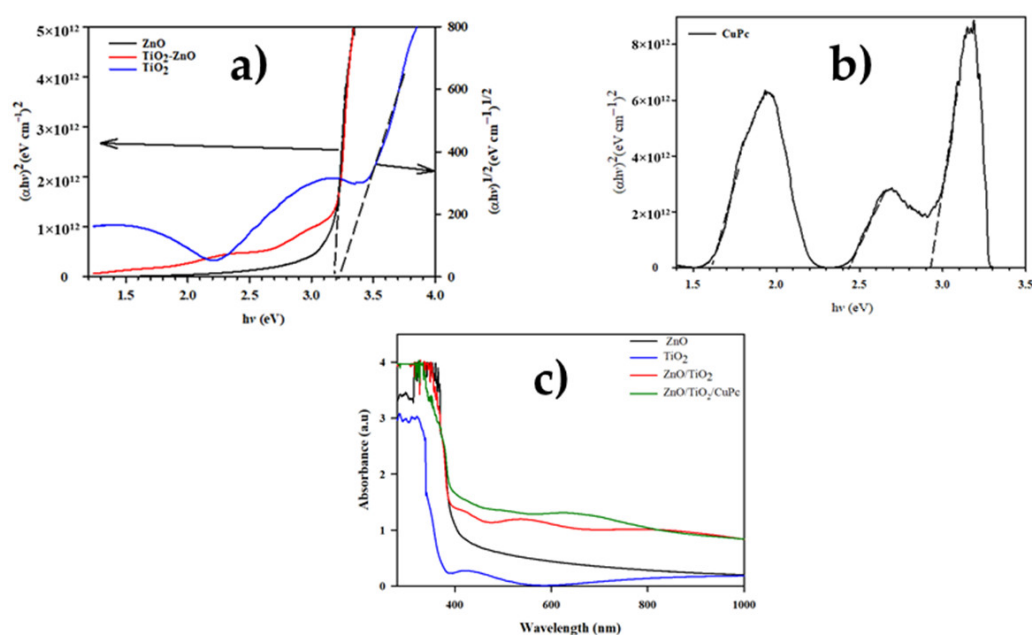


Figure 5. Tauc's plots for energy band gaps (E_g) of (a) TiO₂, ZnO, and TiO₂/ZnO structures, (b) CuPc grown on quartz substrates, and (c) their respective UV-Vis absorption spectra measurements.

For the CuPc layer, energy bandgap (E_g) values were extrapolated as 1.6 eV, 2.44 eV, and 2.92 eV. All are in agreement with previously reported E_g data for CuPc [50,51]. These values are very close to the E_g value we recently reported for silicon phthalocyanine sensitized boron/sodium fluoride modified TiO_2 [3]. In relation to the above, the optical absorption spectra results presented in (Figure 5c) agree with the derived energy band gap (E_g) values of the samples (Figure 5a,b). Thus, with the introduction of ZnO layer on TiO_2 and the additional topcoat of CuPc, extended UV-visible absorption was observed leading to a reduced energy band gap of $\text{TiO}_2/\text{ZnO}/\text{CuPc}$ heterostructure in comparison to the other samples.

3.2.5. Steady-State Photoluminescence Measurement

Figure 6 represents room temperature photoluminescence (RTPL) data of TiO_2 thin films, ZnO rods, TiO_2/ZnO bilayer, and $\text{TiO}_2/\text{ZnO}/\text{CuPc}$ heterostructure grown on quartz substrates. TiO_2 thin films show no UV peak, only a weak emission in the range of 400–450 nm (violet region) that might be emanating from the surface state emissions [52]. However, ZnO rods exhibit a UV peak at 378 nm that is related to near band edge emission because of the recombination of excitons [53]. ZnO rods also display a broad deep level emission (DLE) ranging from 400 nm to 700 nm, which is attributed to the intrinsic defects including oxygen vacancies, oxygen interstitials, zinc ion vacancies and interstitials [54]. It is observed that TiO_2/ZnO bilayer shows no UV peak. It is expected that the underlying TiO_2 layer has some structural defects that behave as traps to capture photo-excited electrons and hence, prevent electron-hole recombination which led to the suppression of the UV peak [55]. However, an enhancement was observed in the DLE intensity for TiO_2/ZnO bilayer compared to ZnO and TiO_2 samples. This increase could originate from the synergy of ZnO and TiO_2 layers, resulting in an increment in the population of intrinsic defects as mentioned above, which is in good agreement with work previously reported [48]. $\text{TiO}_2/\text{ZnO}/\text{CuPc}$ heterostructure indicates a PL plot that is very similar to that of ZnO rods but of a different intensity. The heterostructure showed a lower PL intensity than ZnO-based layers that could be ascribed to the non-radiative recombination induced by CuPc layer. This means a lower charge recombination rate and thus, indicating a potential for better photocatalytic performance [56], as it will be discussed in the next sections.

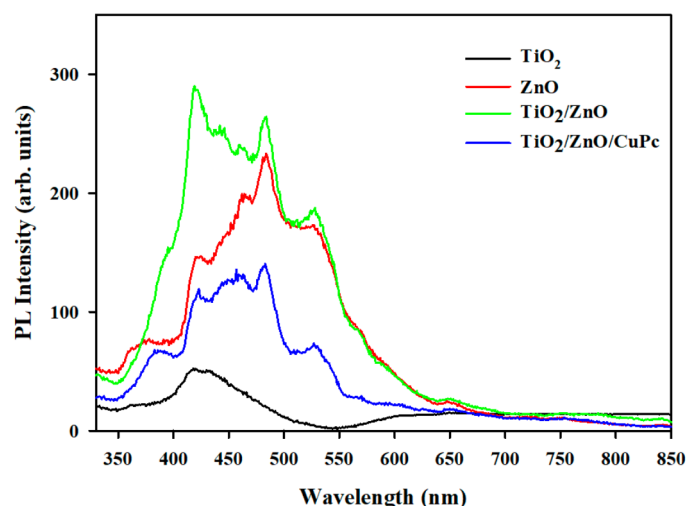


Figure 6. Photoluminescence plots of TiO_2 (black line), ZnO (red line), TiO_2/ZnO (green line), and $\text{TiO}_2/\text{ZnO}/\text{CuPc}$ (blue line).

3.3. Photocatalytic Activity

The photocatalytic activity evaluation of the on stainless steel prepared structures is presented in Figure 7. It was performed on solutions of 5 mg/L ibuprofen concentration. Under natural pH condition of 6.65, TiO_2 film photocatalyst removed about 18% of ibupro-

fen during the 4 h of 365 nm UV irradiation. With TiO₂/ZnO topcoat, ca. 44% ibuprofen was removed at 4 h irradiation under natural pH condition of 6.64. The TiO₂/ZnO/CuPc photocatalyst heterostructure removed about 80% ibuprofen under natural pH condition of 6.5 during the 4 h irradiation time window. With a degradation rate constant of 0.42 h⁻¹, TiO₂/ZnO/CuPc heterostructure was the best performing photocatalyst in comparison to TiO₂ and TiO₂/ZnO structures with respective degradation rate constants of 0.06 h⁻¹ and 0.15 h⁻¹ during the 4 h irradiation time exposure (Figure 7a,b).

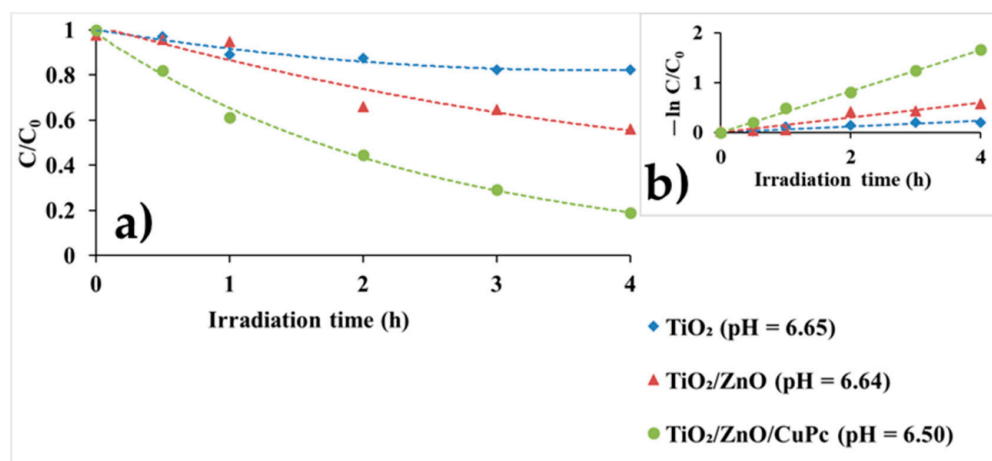


Figure 7. Photocatalytic degradation of 5 mg/L Ibuprofen by (a) TiO₂, TiO₂/ZnO, and TiO₂/ZnO/CuPc at respective natural pH values, and (b) corresponding degradation rate constant.

From the degradation trend of the photocatalyst structures on ibuprofen, it is noteworthy that the modification of TiO₂ films with ZnO layer enhanced TiO₂ photocatalytic efficiency. Further improvement was achieved by CuPc presence on the TiO₂/ZnO topcoat reaching the highest removal rate of the initial 5 mg/L ibuprofen (IBF).

Effects of photolysis as well dark test on the degradation of IBF by the TiO₂/ZnO/CuPc photocatalyst over the investigated 4h irradiation time window did not reflect any significant influence with just about 20% IBF removed for both processes (Figure 8).

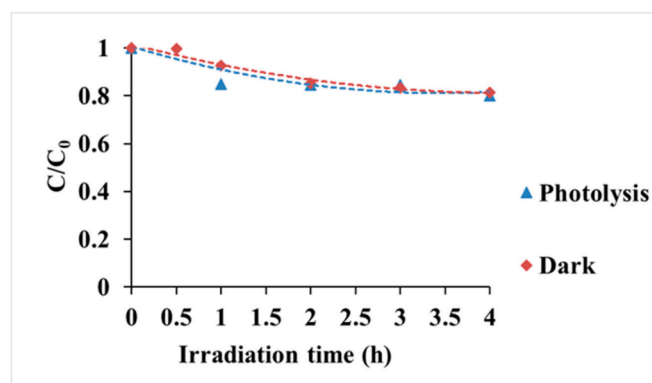


Figure 8. Dark effect with TiO₂/ZnO/CuPc photocatalyst, and photolysis influence on the degradation of IBF ($C_0 = 5$ mg/L, pH = 6.50).

3.3.1. pH Effects

pH condition as an operational parameter for wastewater treatment is crucial [57]. For this reason, in addition to the tested unmodified natural pH = 6.50 of TiO₂/ZnO/CuPc photocatalyst, other pH values of 3, 5, 6, and 9 were also tested (Figure 9). The presented result in Figure 9, shows a trend where IBF degradation by the catalyst follows the order: pH = 6.50 (Natural) > pH = 3 > pH = 9 > pH = 6 > pH = 5. At pH = 3, the photocatalyst removed about 54% IBF after 4 h of irradiation as compared to the unmodified pH = 6.50

(natural) at which about 80% IBF was removed by the photocatalyst. Under alkaline and mild acidic pH values of 9 and 6 respectively, the photocatalyst removed 25% and 23% IBF after 4 h of irradiation, respectively. At a pH = 5, the lowest IBF degradation was observed and the photocatalyst removed just about 9%. IBF pKa value is within 4.52–4.9 [58] and can be linked to the pH effects on the catalyst performance. With pH values above the pKa range, anionic IBF species will be predominant [57]. This predominant species was most favored at aqueous pH value of 6.50 (natural) at which efficient photocatalytic degradation of IBF occurred. Carboxylic group of ibuprofen has been reported to reach the ionized state form of ion-dipole bonds with water molecule at pH values higher than IBF pKa [59,60].

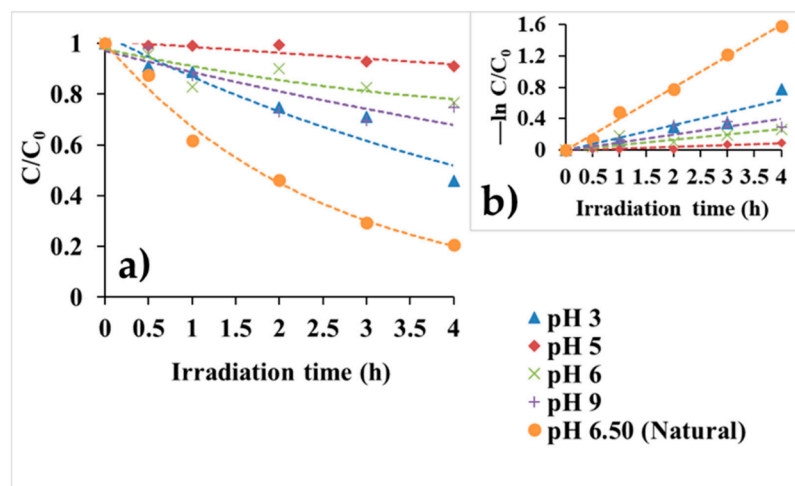


Figure 9. (a) pH effects on $\text{TiO}_2/\text{ZnO}/\text{CuPc}$ catalyst degradation efficiency for IBF ($C_0 = 5 \text{ mg/L}$) removal, and (b) corresponding degradation rate constant.

In comparison to pH 6.50 with the best catalyst performance, pH = 6 and pH = 9 did not favor a considerable IBF degradation rate removal because of IBF anion repulsion with respect to surface properties of the catalyst at such mild and advanced pH alkaline pH conditions. Conditions of pH = 5 showed the least IBF degradation rate of removal most probably due to the incomplete dissociation of IBF into its anionic form disabling favorable electrostatic interactions. A bit of prominence in degradation rate removal witnessed at pH 3 has been attributed to dominant dispersive interactions leading to a higher surface adsorption capacity onto the catalyst surface for removal [60]. Other likely reason might be due to the fact that such a highly acidic pH condition facilitates the generation of reactive species (HO_2 etc.), that promote the photodegradation process in the long run.

As it will be shown in the next Section 3.3.2 the process is significantly affected by such active species. Further catalytic testing was performed under pH = 6.50 at which catalyst showed the best performance.

3.3.2. Effects of Chemical Scavengers

In order to identify the main active species generated during IBF degradation, radical trapping investigations were carried out by introducing chemical scavengers into the working solution containing the catalyst. Benzoquinone (BQ: a superoxide anion $\bullet\text{O}_2^-$ scavenger), isopropyl alcohol (IPA: a hydroxyl radical $\bullet\text{OH}$ scavenger), ethylene-diamine-tetra acetic acid (EDTA: a hole h^+ scavenger), and sodium sulphate (Na_2SO_4 : an electron e^- scavenger) were employed [61].

As presented in Figure 10, the added chemical scavengers in comparison to no scavenger control, suppressed the degradation rate of IBF pollutant by the photocatalyst. In the presence of BQ, IPA, EDTA, and Na_2SO_4 ; IBF degradation percentages were recorded as 29%, 22%, 41%, and 53% respectively. By this result, the imposed radical effect on the investigated photocatalytic degradation of IBF was of the order: $\bullet\text{OH} > \bullet\text{O}_2^- > \text{h}^+ > \text{e}^-$. This suggests that hydroxyl radical ($\bullet\text{OH}$) was ultimately involved in IBF degradation

in addition to the superoxide anion ($\bullet\text{O}_2^-$) which also showed suppressive effect. Both radicals have been practically generated from valence band holes (h^+_{vb}), and conduction band electrons (e^-_{cb}). This makes more feasible a general participation of all the tested radical species even as they depressed IBF percentage degradation with respect to the no scavenger test control (Figure 10).

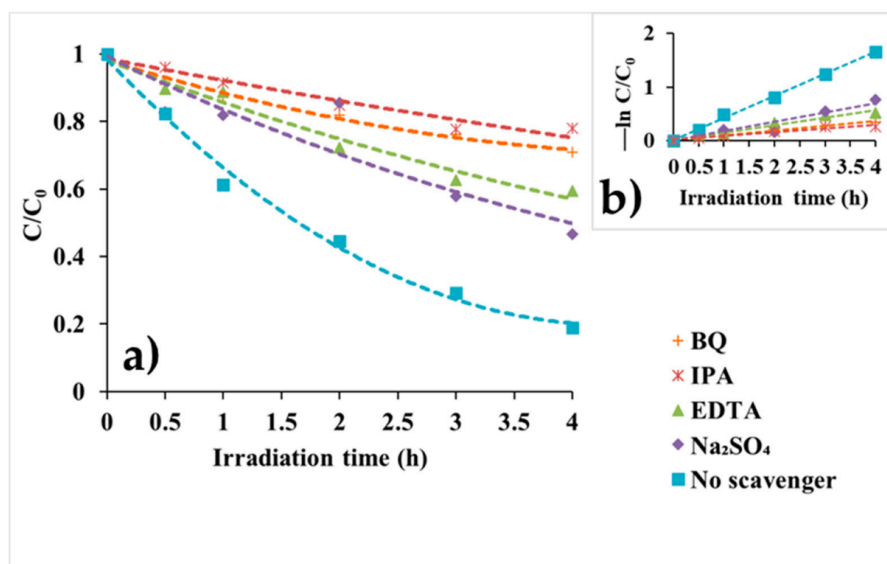


Figure 10. (a) Effects of chemical scavengers on $\text{TiO}_2/\text{ZnO}/\text{CuPc}$ photocatalyst degradation efficiency of IBF ($C_0 = 5 \text{ mg/L}$, $\text{pH } 6.50$), and (b) corresponding degradation rate constant.

3.3.3. Photostability of $\text{TiO}_2/\text{ZnO}/\text{CuPc}$

Reusability of the $\text{TiO}_2/\text{ZnO}/\text{CuPc}$ photocatalyst for the degradation of ibuprofen (IBF) was tested over a five successive cycle tests with result presented in Figure 11.

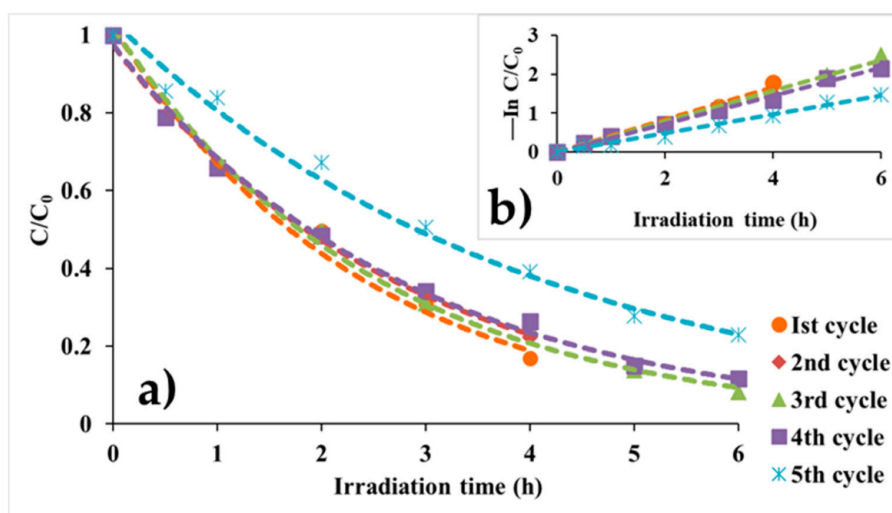


Figure 11. (a) Stability test for IBF ($C_0 = 5 \text{ mg/L}$, $\text{pH} = 6.50$) degradation over $\text{TiO}_2/\text{ZnO}/\text{CuPc}$ photocatalyst, and (b) corresponding degradation rate constant after five cycles.

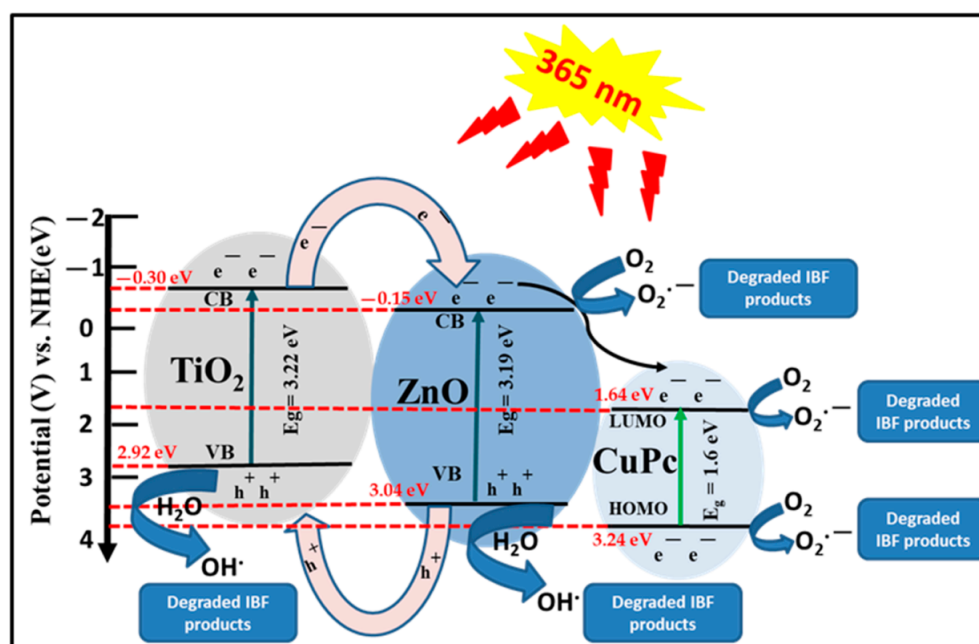
From the Figure 11, it can be observed that the photocatalyst during 4 h irradiation period degraded about same amount of IBF at 80% during the 1st and 2nd cycle runs. With an extended irradiation time window up to 6 h on the 3rd and 4th cycle, a further degradation removal was observed. In the extra 2 h irradiation, about 90% IBF degradation was achieved in both cases with a negligible decline in the 4th cycle (Figure 11).

After the 5th cycle run, a noticeable decline in IBF removal with respect to the other cycle runs occurred; with about 77% IBF removed after 6 h of irradiation during this cycle.

In general, the photocatalyst maintained photostability over IBF degradation during 4 h and extended 6 h irradiation. The slight loss of activity of the photocatalyst at the 5th successive run can be attributed to spallation issues of the ZnO/CuPc topcoat layers in the TiO₂/ZnO/CuPc photocatalyst heterostructure [41]. However, this did not alter to a noticeable extent the structural properties of the photocatalyst as can be seen from (Figure S5) with the XRD pristine state phase of the photocatalyst structure retained after five successive cycle runs. Further confirmation of the minor or no surface structure modification can also be observed by the SEM images obtained from randomly selected 3rd and 5th cycle tests (Figure S6). In comparison with the as prepared SEM surface morphology (Figure 4), the insignificant difference in values between the elemental composition of the photocatalyst heterostructure underline the observed catalyst stability throughout the tested cycles (Figure 11 and Figure S6).

3.3.4. Possible Photodegradation Mechanism of TiO₂/ZnO/CuPc

Based on the investigated reactive oxygen species (ROS) involvement over the degradation of IBF by the TiO₂/ZnO/CuPc photocatalyst (Figure 9), a proposed surface reaction mechanism was deduced (Scheme 2). Suppression of photocatalyst degradation ability over IBF has been higher for hydroxyl (•OH) and superoxide anion (•O₂⁻) radical species (Figure 10).



Scheme 2. Possible photodegradation mechanism of TiO₂/ZnO/CuPc photocatalyst.

However, as the generation of both species rarely exclude the involvement of valence band holes (h⁺_{vb}) and conduction band electrons (e⁻_{cb}) in the photooxidation of organic compounds, participation of classical reactive oxygen species in driving the reaction mechanism has been suggested [2]. Hence, from Figure 9, the investigated species (•OH, •O₂⁻, h⁺, e⁻), all came up with significant suppression effect on the IBF degradation as compared to no chemical scavenger presence.

Upon the irradiation of the TiO₂/ZnO/CuPc photocatalyst, parts of the irradiated TiO₂ thin film due to favored thermodynamic energetics initiated a drift of conduction band electrons (e⁻_{cb}) into the conduction band (CB) of ZnO. In a probable simultaneous path, the valence band holes (h⁺_{vb}) of the ZnO migrate into the valence band (VB) of TiO₂ (Scheme 2). Accordingly, the top layer CuPc because of their intrinsic p-type solid state

semiconductor nature will accept the cascading electrons from the ZnO interface into its CB level.

Thus, the separated charges of conduction band electrons (e^-_{cb}) and valence band holes (h^+_{vb}) at the respective interface layers of the CB and VB heterojunctions are able to combine efficiently with surface molecular oxygen (O_2) and surface adsorbed water molecules generating the respective superoxide anion ($\bullet O_2^-$) and hydroxyl ($\bullet OH$) radical species for IBF degradation. The involved redox reactions ($O_2/\bullet O_2^-$ and $H_2O/\bullet OH$) and even the possible pathway of radical species mechanism generation involving ($O_2 + H^+/\bullet O_2^-$) and ($^-OH/\bullet OH$) can further be supported by the obtained band edge potentials of the heterostructure. From Scheme 2, the CB edge (-0.15 eV) of ZnO is negative enough in comparison to $E^\circ (O_2/\bullet O_2^-)$ of value -0.046 eV vs. NHE. Hence, electrons at this level are favored to interact with the surface oxygen yielding superoxide anion ($\bullet O_2^-$) via one electron reducing reaction [62]. At the CuPc phase, the generation of superoxide anion ($\bullet O_2^-$) at the lowest unoccupied molecular orbital (LUMO) CB level with cascade of electron flows from ZnO CB level is also favored as the 1.64 eV band edge potential is positive enough as compared to the $E^\circ (O_2/\bullet O_2^-)$ of value 0.68 eV vs. NHE required for the generation of the superoxide anion ($\bullet O_2^-$) via the ($O_2 + H^+/\bullet O_2^-$) pathway. Similarly, the highest occupied molecular orbital (HOMO) valence band level of CuPc layer with a band edge potential of 3.24 eV was also favored for the generation of the superoxide anion ($\bullet O_2^-$) via the ($O_2 + H^+/\bullet O_2^-$) pathway (Scheme 2).

On the other hand, the valence band (VB) edge potentials of TiO_2 and ZnO with respective band edge potentials of 2.92 eV and 3.04 eV were favored for the generation of hydroxyl ($\bullet OH$) radicals via possible pathway mechanisms of either ($^-OH/\bullet OH$) or ($H_2O/\bullet OH$) (Scheme 2). This is due to the fact that their edge potentials were positive enough to offset the $E^\circ (^-OH/\bullet OH)$ of value 1.99 eV and that of $E^\circ (H_2O/\bullet OH)$ of value 2.38 eV vs. NHE (Scheme 2).

The interaction of dissolved oxygen molecule and singlet oxygen (1O_2) with the conduction band electrons (e^-_{cb}) of excited CuPc molecule upon irradiation for subsequent yield of the superoxide anion ($\bullet O_2^-$) radical and related hydroperoxyl radicals ($HO_2\bullet$) for eventual hydroxyl ($\bullet OH$) radical species generation is also assumed. As such, it may have an active role during IBF degradation [63]. The steady-state photoluminescence (PL) measurement at room temperature is in favor of the proposed mechanism of the photocatalyst activity. It confirms the proposed facilitated charge transfer/separation mechanism (Scheme 2) of suppressed electrons/holes recombination tendency (Figure 6), which corresponds to the relatively improved photocatalytic activity of the $TiO_2/ZnO/CuPc$ heterostructure.

4. Conclusions

The combined methodology of sol-gel, spray pyrolysis, and spin coating for respective synthesis of TiO_2 , ZnO, and CuPc (produced via Schiff base process) proved successful for the fabrication of $TiO_2/ZnO/CuPc$ heterostructured thin film on stainless steel substrate.

The as-deposited $TiO_2/ZnO/CuPc$ heterostructure was characterized accordingly by several structural/morphological and elemental analytical techniques such as XRD, FTIR, SEM, UV-vis spectroscopy, RTPL, $^1H/^{13}C$ -NMR, and MALDI-TOF. The application of $TiO_2/ZnO/CuPc$ for photocatalytic degradation of ibuprofen (5 mg/L), under $pH = 6.50$, showed an 80% IBF degradation in comparison to 18% and 44% removals for the widely studied TiO_2 and TiO_2/ZnO binary oxide system respectively after 4 h of 365 nm UV irradiation. Photolysis and dark experimental tests showed insignificant contribution over the degradation of IBF. pH influence varied with the photocatalyst degrading 54% IBF at highly acidic $pH = 3$, 25% at alkaline $pH = 9$, 23% at mild acidic $pH = 6$, and a much lower degradation rate of 9% at moderate acidic $pH = 5$. Investigation on the effect of reactive oxygen species (ROS) in the photocatalytic degradation of IBF showed that hydroxyl radical ($\bullet OH$) and superoxide anion ($\bullet O_2^-$) species were the most influential in driving the photooxidation of IBF. With an overall observed trend of $\bullet OH > \bullet O_2^- > h^+ > e^-$

for the reactive species roles, a photodegradation mechanism was proposed. For a low photoluminescence intensity, suppressed charge recombination as well as extended UV-visible absorption was observed by synergy among the TiO₂ and ZnO phases coupled with the non-radiative CuPc top layer. Thus, the heterostructure favored the low energy band gap, and an overall improved photocatalyst activity. The best performing TiO₂/ZnO/CuPc photocatalyst was tested for stability after 4 h and extended 6-h irradiation time. A high IBF degradation efficiency was maintained after five successive cycle runs. The photocatalyst maintained for the 1st and 2nd cycle runs an impressive 80% IBF degradation after 4 h irradiation. At 3rd and 4th cycle runs, and at extended 6 h irradiation, the photocatalyst reached about 90% IBF removal and showed a small decline in activity profile at the 5th cycle run reaching 77% IBF degradation.

In the future, the promising performances of TiO₂/ZnO/CuPc under UV will be tested in the visible and or near infrared (NIR) region for photocatalytic activity over other contaminant of emerging concerns (CEC) compound abatement in water. Furthermore, it will be interesting to investigate the charge transfer mechanisms of such recoverable phthalocyanine sensitized binary oxide systems for organic compound photocatalytic degradation as well as other applications.

Supplementary Materials: The following are available online at <https://www.mdpi.com/2297-8739/8/3/24/s1>, Figure S1: 1H-NMR spectrum of compound (3) in DMSO, Figure S2: 13C-NMR spectrum of compound (3) in DMSO, Figure S3: ESI-MS spectrum of compound (3), Figure S4: MALDI-MS spectrum of compound (4), Figure S5: XRD image of TiO₂/ZnO/CuPc photocatalyst after five (5) consecutive cycle runs, Figure S6: SEM image of TiO₂/ZnO/CuPc photocatalyst after at random selected: (a) 3rd, and (b) 5th cycle runs.

Author Contributions: Conceptualization, C.B., E.B., and I.D.; methodology, C.B., E.B., and T.K.; software, C.B., E.B.; I.D.; validation, C.B.; E.B. and T.K.; formal analysis, V.N.S.; investigation, C.B.; resources, C.B.; I.A.; E.B.; T.K.; S.Y.; data curation, C.B.; writing—original draft preparation, C.B.; S.Y.; writing—review and editing, V.N.S.; E.B.; I.A.; I.D.; T.K.; S.Y.; visualization, I.A.; supervision, E.B.; V.N.S.; I.A.; project administration, E.B.; I.A.; funding acquisition, E.B.; I.A. All authors have read and agreed to the published version of the manuscript.

Funding: This research was funded by the EUROPEAN UNION'S HORIZON 2020 RESEARCH AND INNOVATION PROGRAMME under the MARIE SKŁODOWSKA -CURIE grant No: 765860 (AQUALity).

Institutional Review Board Statement: Not applicable.

Informed Consent Statement: Not applicable.

Data Availability Statement: The Data presented in this study are available in [Immobilized TiO₂/ZnO Sensitized Copper (II) Phthalocyanine Heterostructure for the Degradation of Ibuprofen Under UV Irradiation and in the supplementary information: Immobilized TiO₂/ZnO Sensitized Copper (II) Phthalocyanine Heterostructure for the Degradation of Ibuprofen Under UV Irradiation].

Conflicts of Interest: The authors declare no conflict of interest.

References

1. Shahawi, M.S.E.; Hamza, A.; Bashammakh, A.S.; Al-Saggaf, W.T. An Overview on the Accumulation, Transformations, Toxicity, and Analytical Methods for the Monitoring of Persistent Organic Pollutants. *Talanta* **2010**, *80*, 1587–1597. [CrossRef]
2. Anucha, C.B.; Altin, I.; Biyiklioglu, Z.; Bacaksiz, E.; Polat, I.; Stathopoulos, V.N. Synthesis, Characterization, and Photocatalytic Evaluation of Manganese (III) Phthalocyanine Sensitized ZnWO₄ (ZnWO₄MnPc) for Bisphenol A Degradation under UV Irradiation. *Nanomaterials* **2020**, *10*, 2139. [CrossRef]
3. Anucha, C.B.; Altin, I.; Fabbri, D.; Degirmencioglu, I.; Calza, P.; Magnacca, G.; Stathopoulos, V.N.; Bacaksiz, E. Synthesis and Characterization of B/NaF and Silicon Phthalocyanine-Modified TiO₂ and an Evaluation of Their Photocatalytic Removal of Carbamazepine. *Separations* **2020**, *7*, 71. [CrossRef]
4. Holgado, C.J.; Crimatopoulos, C.; Stathopoulos, V.N.; Sakkas, V. Investigating the Utility of Fabric Phase Sorptive Extraction and HPLC-UV-Vis/DAD to Determine Antidepressant Drugs in Environmental Aqueous Samples. *Separations* **2020**, *7*, 39. [CrossRef]
5. Scheneider, J.; Matsuoka, M.; Takeuchi, M.; Zhang, J.; Horiuchi, Y.U.; Anpo, M.; Bahnemann, D.W. Understanding TiO₂ Photocatalysis: Mechanisms and Materials. *Chem. Rev.* **2014**, *114*, 9919. [CrossRef] [PubMed]

6. Linsebigler, A.L.; Guangquang, L.; Yates, J.T. Photocatalysis on TiO₂ Surfaces: Principles, Mechanisms, and Selected Results. *Chem. Rev.* **1995**, *95*, 735–758. [[CrossRef](#)]
7. Shahrezaei, M.; Babaluo, A.A.; Habibzadeh, S.; Haghghi, M. Photocatalytic Properties of 1D TiO₂ Nanostructures Prepared from Polyacrylamide Gel- TiO₂ Nanopowders by Hydrothermal Synthesis. *Eur. J. Inorg. Chem.* **2017**, *3*, 694–703. [[CrossRef](#)]
8. Kment, S.; Riboni, F.; Pausova, S.; Wang, L.; Han, H.; Hubicka, Z.; Krysa, J.; Schumuki, P.; Zboril, R. Photoanodes Based on TiO₂ and α -Fe₂O₃ for Water Splitting- Superior Role of 1D Nanoarchitectures and of Combined Heterostructures. *Chem. Soc. Rev.* **2017**, *46*, 3716–3769. [[CrossRef](#)]
9. Dal Santo, V.; Naldoni, A. Titanium Dioxide Photocatalysis. *Catalysts* **2018**, *8*, 591. [[CrossRef](#)]
10. Pandis, P.K.; Perros, D.E.; Stathopoulos, V.N. Doped Apatite-Type Lanthanum Silicates in CO Oxidation Reaction. *Catal. Commun.* **2018**, *114*, 98–103. [[CrossRef](#)]
11. Damaskinos, C.M.; Vasiliades, M.A.; Stathopoulos, V.N.; Efstathiou, A.M. The Effect of CeO₂ Preparation Method on the Carbon Pathways in the Dry Reforming of Methane on Ni/CeO₂ Studied by Transient Techniques. *Catalysts* **2019**, *9*, 621. [[CrossRef](#)]
12. Stefa, S.; Lykaki, M.; Binas, V.; Pandis, P.K.; Stathopoulos, V.N.; Konsolakis, M. Hydrothermal Synthesis of ZnO-Doped Ceria Nanorods: Effects of ZnO Content on the Redox Properties and the CO Oxidation of Performance. *Appl. Sci.* **2020**, *10*, 7605. [[CrossRef](#)]
13. Lykaki, M.; Stefa, S.; Carabiniero, S.A.C.; Pandis, P.K.; Stathopoulos, V.N.; Konsolakis, M. Facet-Dependent Reactivity of Fe₂O₃/CeO₂ Nanocomposites: Effect of Ceria Morphology on CO Oxidation. *Catalysts* **2019**, *9*, 371. [[CrossRef](#)]
14. Stefa, S.; Lykaki, M.; Fragkoulis, D.; Binas, V.; Pandis, P.K.; Stathopoulos, V.N.; Konsolakis, M. Effect of the Method of Preparation on the Physicochemical Properties and the CO Oxidation Performance of the Nanostructured CeO₂/TiO₂ Oxides. *Processes* **2020**, *8*, 847. [[CrossRef](#)]
15. Ge, M.; Cao, C.; Huang, J.; Li, S.; Chen, Z.; Zhang, K.-Q.; Al-Deyab, S.S.; Lai, Y. A Review of One-Dimensional TiO₂ Nanostructured Materials for Environmental and Energy Applications. *J. Mater. Chem. A* **2016**, *4*, 6772–6801. [[CrossRef](#)]
16. Fujishima, A.; Rao, T.N.; Tyrk, D.A. Titanium dioxide Photocatalysis. *J. Photochem. Photobiol. C Photochem. Rev.* **2000**, *1*, 1–21. [[CrossRef](#)]
17. Garcia, N.M.; Ignacio Maldonado, M.; Coronado, J.M.; Malato, S. Degradation Study of 15 Emerging Contaminants at Low Concentration by Immobilized TiO₂ in a Plant. *Catal. Today* **2010**, *151*, 107–113. [[CrossRef](#)]
18. Srikanth, B.; Goutham, R.; Naraya, B.; Ramprasath, A.; Gopinath, K.P. Recent Advancements in Supporting Materials for Immobilized Photocatalytic Applications in Wastewater Treatment. *J. Environ. Manag.* **2017**, *200*, 60–78. [[CrossRef](#)]
19. Mofokeng, M.J.; Kumar, V.; Kroon, R.E.; Ntwaeaborwa, O.M., J. Structure and Optical Properties of Dy³⁺ Activated Sol-Gel ZnO-TiO₂ Nanocomposites. *J. Alloy Compd.* **2017**, *711*, 121–131. [[CrossRef](#)]
20. Siwinska, K.S.; Kubiak, A.; Piasecki, A.; Goscianska, J.; Nowaczyk, G.; Jurga, S.; Jesionowski, T. TiO₂-ZnO Binary Oxide Systems: Comprehensive Characterization and Tests of Photocatalytic Activity. *Materials (Basel)* **2018**, *11*, 841. [[CrossRef](#)]
21. Perovic, K.; de la Rosa, F.M.; Kovacic, M.; Kusic, H.; Stangar, U.L.; Fresno, F.; Dionysiou, D.D.; Bozic, A.L. Recent Achievements in Development of TiO₂-Based Composite Photocatalytic Materials for Solar Driven Water Purification and Water Splitting. *Materials* **2020**, *13*, 1338. [[CrossRef](#)]
22. Zhou, X.; Shi, T.; Zhou, H. Hydrothermal Preparation of ZnO-Reduced Graphene Oxide Hybrid with High Performance in Photocatalytic Degradation. *App. Surf. Sci.* **2012**, *258*, 6204–6211. [[CrossRef](#)]
23. Kuo, M.-Y.; Hsiao, C.-F.; Chiu, Y.-H.; Lai, T.-H.; Fang, M.-J.; Wu, J.-Y.; Chen, J.-W.; Wu, C.-L.; Wei, K.-H.; Lin, H.-C.; et al. Au@Cu₂O Core@Shell Nanocrystals as Dual-Functional Catalysts for Sustainable Environmental Applications. *Appl. Catal. B Environ.* **2019**, *242*, 499–506. [[CrossRef](#)]
24. Chiu, Y.-H.; Hsu, Y.-Y. Au@Cu₇S₄ Yolk @ Shell Nanocrystal-Decorated TiO₂ Nanowires as an All-Day-Active Photocatalyst for Environmental Purification. *Nano Energy* **2017**, *31*, 286–295. [[CrossRef](#)]
25. Sardar, S.; Kar, P.; Pal, S.K. The Impact of Central Metal Ions in Porphyrin Functionalized ZnO/TiO₂ for Enhanced Solar Energy Conversion. *J. Mater. Nanosci.* **2014**, *1*, 12–30.
26. Albay, C.; Koc, M.; Altin, I.; Bayrak, R.; Degirmencioglu, I.; Sokmen, M. New Dye Sensitized Photocatalyst: Copper (II) Phthalocyanine/TiO₂ Nanocomposite for Water Remediation. *J. Photochem. Photobiol. A Chem.* **2016**, *324*, 117–125. [[CrossRef](#)]
27. Cabir, B.; Yurderi, M.; Caner, N.; Agirtas, M.S.; Zahmakiran, M.; Kaya, M. Methylene Blue Photocatalytic Degradation under Visible Light Irradiation on Copper Phthalocyanine-Sensitized TiO₂ Nanopowders. *Mater. Sci. Eng. B* **2017**, *224*, 9–17. [[CrossRef](#)]
28. Vallejo, W.A.; Uribe, C.D.; Guzman, A.E.C. Methylene Blue Photocatalytic Degradation Under Visible Irradiation on TiO₂ Thin films Sensitized with Cu and Zn Tetracarboxy-Phthalocyanines. *J. Photochem. Photobiol. A Chem.* **2015**, *299*, 80–86. [[CrossRef](#)]
29. Li, M.; Hu, Q.; Shan, H.; Yu, W.; Xu, Z.-X. Fabrication of Copper Phthalocyanine/Reduced Graphene Oxide Nanocomposite for Efficient Reduction of Hexavalent Chromium. *Chemosphere* **2021**, *263*, 128250. [[CrossRef](#)] [[PubMed](#)]
30. Li, K.; Pang, Y.; Lu, Q. In situ Growth of Copper (ii) Phthalocyanine-Sensitized Electrospun CeO₂/Bi₂MoO₆ Nanofibres: A Highly Efficient Photoelectrocatalyst towards Degradation of Tetracycline. *Inorg. Chem. Front.* **2019**, *6*, 3215–3224. [[CrossRef](#)]
31. Mun, S.J.; Park, S.-J. Graphitic Carbon Nitride Materials for Photocatalytic Hydrogen Production via Water Splitting: A Short Review. *Catalysts* **2019**, *9*, 805. [[CrossRef](#)]
32. Lee, S.L.; Chang, C.-J. Recent Progress on Metal Sulfide Composite Nanomaterials for Photocatalytic Hydrogen Production. *Catalyst* **2019**, *9*, 457. [[CrossRef](#)]

33. Fang, M.-J.; Tsao, C.-W.; Hsu, Y.-J. Semiconductor Nanoheterostructures for Photoconversion Applications. *J. Phys. D Appl. Phys.* **2020**, *53*, 143001. [[CrossRef](#)]
34. Ge, J.; Zhang, Y.; Heo, Y.-J.; Park, S.-J. Advanced Design and Synthesis of Composite Photocatalysts for the Remediation of Wastewater: A Review. *Catalyst* **2019**, *9*, 122. [[CrossRef](#)]
35. Devi, A.S.; Aswathy, V.V.; Sheena Mary, Y.; Panicker, C.Y.; Armakovic, S.J.; Ravindran, R.; van Alsenoy, C. Synthesis, XRD Crystal Structure Analysis, Vibrational Spectral Analysis, Molecular Dynamics and Molecular Docking Studies of 2-(3-methoxy-4-hydroxyphenyl) benzothiazole. *J. Mol. Struct.* **2017**, *1148*, 282–292. [[CrossRef](#)]
36. Yilmaz, S.; Polat, I.; Atasoy, Y.; Bacaksiz, E. Structural, Morphological, Optical and Electrical Evolution of Spray Deposited ZnO Rods Co-doped with Indium and Sulphur Atoms. *J. Mater. Sci. Mater. Electron.* **2014**, *25*, 1810–1816. [[CrossRef](#)]
37. Chohan, S.; Booyesen, I.N.; Mambanda, A. Cobalt b-tetra(3-oxyflavone/2-(2-oxyphenyl) benzoxazole) phthalocyanines and Their Carbon Nanotube Conjugates: Formation, Characterization and Dopamine Electrocatalysis. *Polyhedron* **2015**, *102*, 284–292. [[CrossRef](#)]
38. Nas, A.; Kantekin, H.; Koca, A. Novel 4-(2-(benzo[d]thiazol-2-yl) phenoxy) Substituted Phthalocyanine Derivatives: Synthesis, Electrochemical and In-situ Spectroelectrochemical Characterization. *J. Organomet. Chem.* **2014**, *757*, 62–71. [[CrossRef](#)]
39. Aktas, A.; Durmus, M.; Degirmencioglu, I. Self-assembly Novel Phthalocyanines Containing a Rigid Benzothiazole Skeleton With a 1,4-Benzene Linker: Synthesis, Spectroscopic and Spectral Properties, and Photochemical/Photophysical Affinity. *Polyhedron* **2012**, *48*, 80–91. [[CrossRef](#)]
40. Elhalil, A.; Elmoubarki, R.; Farnane, M.; Machrouhi, A.; Sadiq, M.; Mahjoubi, F.Z.; Qourzal, S.; Barka, N. Photocatalytic Degradation of Caffeine as a Model Pharmaceutical Pollutant on Mg Doped ZnO-Al₂O₃ Heterostructure. *Environ. Nanotechnol. Monit. Manag.* **2018**, *10*, 63–72. [[CrossRef](#)]
41. Mavric, T.; Valant, M.; Forster, M.; Cowman, A.J.; Lavrencic, U.; Emin, S. Design of Highly Photocatalytically Active ZnO/CuWO₄ Nanocomposite. *J. Colloid Interface Sci.* **2016**, *483*, 93–101. [[CrossRef](#)] [[PubMed](#)]
42. Karkare, M.M. Choice of Precursor Not Affecting the Size of Anatase TiO₂ Nanoparticles but Affecting Morphology under Broader View. *Int. Nano Lett.* **2014**, *4*, 111. [[CrossRef](#)]
43. Bepalko, Y.; Kuzenetsova, T.; Kriger, T.; Chesalov, Y.; Lapina, O.; Ishchenko, A.; Larina, T.; Sadykov, V.; Stathopoulos, V. La₂Zr₂O₇/LaAlO₃ Composite Prepared by Mixing Precipitated Precursors: Evolution of Its Structure under Sintering. *Mater. Chem. Phys.* **2020**, *251*, 123093. [[CrossRef](#)]
44. Balakrishnan, M.; John, R. Properties of Sol-gel Synthesized Multiphase TiO₂ (AB)-ZnO (ZW) Semiconductor Nanostructure: An Effective Catalyst for Methylene Blue Dye Degradation. *Iran. J. Catal.* **2020**, *10*, 1–16.
45. Khan, M.I.; Bhatti, K.A.; Qindeel, R.; Bousiakuo, L.G.; Alonizan, N. Investigations of The Structural, Morphological and Electrical Properties of Multilayer ZnO/TiO₂ Thin films Deposited by Sol-gel Technique. *Results Phys.* **2016**, *6*, 156–160. [[CrossRef](#)]
46. Shaogui, Y.; Xie, Q.; Xinyong, L.; Yazli, L.; Shuo, C.; Guohua, C. Preparation, Characterization and Photoelectrocatalytic Properties of Nanocrystalline Fe₂O₃/TiO₂, ZnO/TiO₂, Fe₂O₃/ZnO/TiO₂ Composite Film Electrodes Towards Pentachlorophenol Degradation. *Phys. Chem. Chem. Phys.* **2004**, *6*, 659–664. [[CrossRef](#)]
47. Wang, Z.; Helmerston, U.; Kall, P.-O. Optical Properties of Anatase TiO₂ Thin Films Prepared by Aqueous Sol-Gel Process at Low Temperature. *Thin Solid Films* **2002**, *405*, 50–54. [[CrossRef](#)]
48. Zhao, L.; Xia, M.; Liu, Y.; Zheng, B.; Jiang, Q.; Lian, L. Structure and Photocatalysis of TiO₂/ZnO Double -Layer Film Prepared by Pulsed Laser Deposition. *Mater. Trans.* **2012**, *53*, 463–468. [[CrossRef](#)]
49. Upadhyay, G.K.; Rajput, J.K.; Pathak, T.K.; Kumar, V.; Purohit, L.P. Synthesis of ZnO: TiO₂ Nanocomposites for Photocatalyst Application in Visible Light. *Vacuum* **2019**, *160*, 154–163. [[CrossRef](#)]
50. Duran, N.E.; Capan, I. A Study on The Macrocyclic Ring Size and R-group Chain Length on The Optical Properties of The CuPc Thin Films. *Indian J. Phys.* **2020**, *94*, 1061–1070. [[CrossRef](#)]
51. Elgazzar, E. Improvement of the Efficiency of Al/CuPc/n-Si/Al Schottky Diode Based on Strong Light Absorption and High Photocarriers Response. *Mater. Res. Express* **2020**, *7*, 095102. [[CrossRef](#)]
52. Mathew, S.; Prasad, A.K.; Benoy, T.; Rakesh, P.P.; Hari, M.; Radhakrishnan, P.; Nampoore, V.P.N.; Vallaban, C.P.G. UV-Visible Photoluminescence of TiO₂ Nanoparticles Prepared by Hydrothermal Method. *J. Fluoresc.* **2012**, *22*, 1563–1569. [[CrossRef](#)]
53. Cai, H.; Liang, P.; Hu, Z.; Shi, L.; Yang, X.; Sun, J.; Xu, N.; Wu, J. Enhanced Photoelectrochemical Activity of ZnO-Coated TiO₂ Nanotubes and Its Dependence on ZnO Coating Thickness. *Nanoscale Res. Lett.* **2016**, *11*, 104. [[CrossRef](#)]
54. Yilmaz, S.; McGlynn, E.; Bacaksiz, E.; Cullen, J.; Chellappan, R.K. Structural, Optical and Magnetic Properties of Ni Doped ZnO Micro-rods Grown by The Spray Pyrolysis Method. *Chem. Phys. Lett.* **2012**, *525-526*, 72–76. [[CrossRef](#)]
55. Zhao, S.; Cheng, Z.; Kang, L.; Li, M.; Gao, Z. The Facile Preparation of Ag Decorated TiO₂/ZnO Nanotubes and Their Potent Photocatalytic Degradation Efficiency. *RSC Adv.* **2017**, *7*, 50064. [[CrossRef](#)]
56. Pant, B.; Ojha, G.P.; Kuk, Y.-S.; Kwon, O.H.; Park, Y.W.; Park, W. Synthesis and Characterization of ZnO-TiO₂/Carbon Fibre Composite with Enhanced Photocatalytic Properties. *Nanomaterials* **2020**, *10*, 1960. [[CrossRef](#)] [[PubMed](#)]
57. Arriaga, F.M.; Palma, R.A.T.; Petrier, C.; Esplugas, S. Ultrasonic Treatment of Water Contaminated with Ibuprofen. *Water Res.* **2008**, *42*, 4243–4248. [[CrossRef](#)]
58. Simsek, E.B.; Kilic, B.; Asgin, M.; Akan, A. Graphene Oxide Based Heterojunction TiO₂-ZnO Catalyst with Outstanding Photocatalytic Performance for Bisphenol A, Ibuprofen, and Flurbiprofen. *J. Ind. Eng. Chem.* **2018**, *59*, 115–126. [[CrossRef](#)]

59. Gongora, J.F.; Elizondo, P.; Ramirez, A.H. Photocatalytic Degradation of Ibuprofen Using TiO₂ Sensitized by Ru (II) Polyaiza Complexes. *Photochem. Photobiol. Sci.* **2017**, *16*, 31. [[CrossRef](#)]
60. Guedid, H.; Reinert, L.; Leveque, J.-M.; Soneda, Y.; Bellakhal, N.; Duclaux, L. The Effects of The Surface Oxidation of Activated Carbon, The Solution pH and The Temperature on Adsorption of Ibuprofen. *Carbon* **2013**, *54*, 432–443. [[CrossRef](#)]
61. Ma, H.-Y.; Zhao, L.; Guo, L.-H.; Zhang, H.; Chen, F.-J.; Yu, W.-C. Roles of Reactive Oxygen Species (ROS) in the Photocatalytic Degradation of Pentachlorophenol and Its Main Toxic Intermediates by TiO₂/UV. *J. Hazard. Mater.* **2019**, *369*, 719–726. [[CrossRef](#)] [[PubMed](#)]
62. Rosman, N.; Salleh, W.N.W.; Aziz, F.; Ismail, A.F.; Harun, Z.; Bahri, S.S.; Nagai, K. Electrospun Nanofibres Embedding ZnO/Ag₂CO₃/Ag₂O Heterojunction Photocatalyst with Enhanced Photocatalytic Activity. *Catalyst* **2019**, *9*, 565. [[CrossRef](#)]
63. Zhang, M.; Shao, C.; Guo, Z.; Zhang, Z.; Mu, J.; Cao, T.; Liu, Y. Hierarchical Nanostructures of Copper (II) Phthalocyanine on Electrospun TiO₂ Nanofibers: Controllable Solvothermal—Fabrication and Enhanced Visible Photocatalytic Properties. *ACS Appl. Mater. Interfaces* **2011**, *3*, 369–377. [[CrossRef](#)] [[PubMed](#)]